Prolate spheroids settling in a quiescent fluid: clustering, microstructures and collisions

Xinyu Jiang[1], Chunxiao Xu[1], Lihao Zhao[1] †

[1]AML, Department of Engineering Mechanics, Tsinghua University, Beijing 100084, China

(Received xx; revised xx; accepted xx)

In the present study, we investigate the settling of prolate spheroidal particles in a quiescent fluid by means of particle-resolved direct numerical simulations. By varying the particle volume fraction (ϕ) from 0.1% to 10%, we observe a non-monotonic variation of particle mean settling velocity with a local maximum at $\phi = 1\%$. To explain this finding, we examine the spatial distribution and orientation of dispersed particles in the present flow system. The statistics of particle-pairs indicate that settling prolate particles tend to form column-like microsturctures, revealing the tendency for prolate particles to be attracted and entrapped in wake-flow regions. The attraction of particles gives rise to the formation of large-scale particle clusters at intermediate particle volume fractions. The most intense particle clustering at $\phi = 1\%$, which is quantified by the standard deviation of Voronoi volume, induces a swarm effect and substantially enhances the particle settling rate by around 25%. While, in the very dilute suspensions with $\phi = 0.1\%$, although the particle microstructure is most pronounced, the tendency of particle clustering is attenuated due to the long inter-particle distance. In the dense suspensions with $\phi \geqslant 5\%$, the crowded particle arrangement leads to the disruption of particle-induced wakes, which breaks particle microstructures and inhibits the particle clustering. Consequently, hindrance effect dominates and reduces the settling speed. Additionally, in contrast to particle spatial distribution, we demonstrate that the particle orientation plays a less important role in particle mean settling velocity. At last, we examine the collision efficiency of settling particles by computing the collision kernel. As ϕ increases, the collision kernel is found to decrease monotonically, which is primarily attributed to the decrease of radial distribution function in dense suspensions. In contrast, the radial relative velocity is almost a constant with the change of ϕ. These results reveal the importance of hydrodynamic interactions, including the wake-flow-induced attractions and the lubrication effect, in collisions among settling spheroids.

1. Introduction

Particle-laden flows are commonly encountered in natural and industrial processes, such as the transport of air or underwater pollution, marine snow generated by settling plankton or microplastics, and precipitation in the atmosphere (Pruppacher & Klett 2010; Guazzelli & Hinch 2011; Trudnowska *et al.* 2021). One of fundamental challenges in these applications is the gravity-driven sedimentation of particles in fluids, which involves complex interactions

† Email address for correspondence: zhaolihao@tsinghua.edu.cn

between moving particles and the carrying fluid flow (Guazzelli & Hinch 2011), as well as collisions among dispersed particles (Ayala *et al.* 2008).

1.1. *Settling of spherical particles*

Understanding the sedimentation of a swarm of particles is based on the studies on the settling motion of a single sphere. Previous studies have revealed that the settling mode and speed of an isolated sphere depend on two dimensionless parameters, namely the particle-to-fluid density ratio α, and the Galileo number Ga, which measures the ratio between the buoyancy force and viscous force acting on the sphere (Jenny *et al.* 2004; Ern *et al.* 2012). In the creeping flow regime, the sphere settles vertically with a constant settling velocity because of the balance between the buoyancy force and the Stokes drag. With the increase of particle settling Reynolds number (defined by $Re_t = V_t D/\nu$, where V_t is the settling velocity, D is the particle diameter, and ν is the fluid kinematic viscosity) to a finite value, the introduction of fluid inertia results in the appearance of rear wake behind the settling sphere. In the inertial regime, with the change of the morphology of rear weak and the particle inertia, a variety of settling modes (including the vertical, oblique, zigzag, helical and chaotic motions) can be observed (Jenny *et al.* 2004; Horowitz & Williamson 2010; Ern *et al.* 2012).

Regarding the settling motion of double particles, the hydrodynamic interaction between the two particles plays an important role. A typical example is the drafting-kissing-tumbling (DKT) process of a pair of settling spheres (Fortes *et al.* 1987; Glowinski *et al.* 2001). Specifically, as for two identical spherical particles with an initial vertical displacement, the settling speed of the trailing particle is accelerated when it resides in the wake of the leading particle. This is because the hydrodynamic drag experienced by the trailing particle is reduced due to the lower pressure in the wake region. As a result, the trailing particle progressively approaches the leading particle (drafting stage). Subsequently, the two particles touch and form an elongated body aligned along the vertical direction (kissing stage). However, settling with this vertically aligned configuration is unstable. Consequently, the particle pair tumbles and separates, with the originally trailing particle becoming the leading one (tumbling stage). In summary, the DKT process reflects complicated the hydrodynamic interaction between a pair of settling particles.

When considering the sedimentation of a large number of particles, the most well-known phenomenon is the hindered settling rate of dispersed particles, namely the reduction of mean settling velocity (denoted by $\langle V_s \rangle$) with the increase of particle volume fraction ϕ. This hindrance effect can be explained as follows. The upward mean flow of the fluid, which compensates for the downward motion of particles, increases the hydrodynamic drag experienced by settling particles (Di Felice 1999). Richardson & Zaki (1954) first proposed an empirical correlation of $\langle V_s \rangle$ in the suspension as a function of ϕ at a low settling Reynolds number. Since then, a series of studies have been carried out to improve the empirical expression of the hindered settling velocity as a function of ϕ and Re_t (Garside & Al-Dibouni 1977; Di Felice 1999; Yin & Koch 2007).

However, in the past two decades, by virtue of the state-of-the-art particle-resolved direct numerical simulation (PR-DNS), several researchers have observed a striking enhancement of $\langle V_s \rangle$ to be greater than V_t (the settling velocity of an isolated particle) in dilute suspensions ($\phi \lesssim 2\%$) at a relatively high Reynolds number ($Re_t \gtrsim 175$) (Kajishima & Takiguchi 2002; Kajishima 2004; Uhlmann & Doychev 2014; Zaidi *et al.* 2014; Zaidi 2018*b*). By looking into the spatial distribution of dispersed particles, the occurrence of enhanced settling velocity is found to be always accompanied with the appearance of column-like particle clusters (Uhlmann & Doychev 2014; Zaidi *et al.* 2014). As particle clusters fall faster than the isolated particle, the overall average settling velocity is enhanced in this regime. These findings have also been experimentally confirmed by Huisman *et al.* (2016), who observed particle clusters and increased settling rate at high Galileo numbers. In addition, Zaidi *et al.* (2014) and Moriche *et al.* (2023) ascribed the formation of particle clusters to the entrapment of particles in the wake regions (similar to the drafting stage in the DKT process of a pair of particles). However, particle clustering and increased settling rate disappear at low Reynolds numbers or high particle volume fractions. On the one hand, if Re_t is not sufficiently high, the wakes behind the settling particles are not intense enough to induce the formation of particle clusters (Zaidi *et al.* 2014). Instead, settling particles tend to form orderly arrangement in this scenario (Yin & Koch 2007; Zaidi *et al.* 2014, 2015). On the other hand, in the suspension with a large ϕ, the small inter-particle distance disrupts the fluid structures and thus inhibits the particle clustering (Zaidi 2018*b*). Consequently, hindrance effect dominates and reduces the average settling velocity of dispersed particles.

1.2. *Settling of non-spherical particles*

In practice, the dispersed particles are commonly non-spherical in shape. For instance, ice crystals in clouds, plankton in the marine, and dusts in the atmosphere are always disk-like or rod-like in shape (Shaw 2003; Mallios *et al.* 2020; Slomka & Stocker 2020). For simplicity, non-spherical particles are often modelled as spheroids, including prolate spheroids to approximate rod-like particles and oblate spheroids for disk-like particles. The rotation and orientation of these spheroids are more complex than that of spheres, and the behavior of non-spherical particles in fluids is highly shape-dependent (Voth & Soldati 2017).

As for a single spheroid settling in a quiescent fluid, the particle maintains its initial orientation in the regime of creeping flow owing to the vanishing hydrodynamic torque. Accordingly, the terminal settling velocity is orientation-dependent (Happel & Brenner 1983). However, when the fluid inertia is taken into account, a non-negligible hydrodynamic torque reorients the settling spheroid to a broad-side-on alignment (Khayat & Cox 1989; Ardekani *et al.* 2016; Dabade *et al.* 2016). Moreover, when the fluid inertia is strong enough to induce the wake instability, the settling motion of the spheroid transitions from the steady vertical falling to complicated unsteady modes. These modes include spiral, zigzag (or fluttering), tumbling, and chaotic motions, and are determined by the aspect ratio, Galileo number and density ratio of the spheroid (Chrust *et al.* 2013; Ardekani *et al.* 2016; Zhou *et al.* 2017).

Moreover, the DKT process between a pair of spheroidal particles is quite different from that of spherical particles. As for a pair of oblate particles with an aspect ratio (the ratio between the polar radius and the equator radius) $\lambda = 1/3$, the two particles do not undergo the tumbling stage after they are attracted and touch. Instead, they fall together with a steady pilled-up configuration, as if they are stuck together (Ardekani *et al.* 2016). Regarding two prolate spheroids with $\lambda = 3$, the DKT process is more complicated and depends on the initial relative orientation between the two particles (Ardekani *et al.* 2016). If the symmetry axes of the two particles are initially parallel, the DKT process of the prolate particle pairs is similar to that of spherical particles. While if the symmetry axes are perpendicular at the beginning, a stable cross configuration is formed and the two prolate particles do not separate for a long time after they touch, similar to the case of the oblate particle pair. In principle, the attraction zone (within which the trailing particle can be attracted by the leading one) is larger, and the interaction time is longer for the DKT process of spheroidal particle pairs compared to that of spherical ones (Ardekani *et al.* 2016; Moriche *et al.* 2023). Therefore, particle shape plays an important role in the hydrodynamic interaction of settling particles.

With regard to the settling of a large number of non-spherical particles, increased settling velocity of elongated fibres was observed in the creeping flow regime due to the formation of particle streamers aligning in the gravitational direction (Kuusela *et al.* 2003; Saintillan *et al.* 2006; Shin *et al.* 2009). However, in the cases with finite fluid inertia, less is known about the settling behavior of non-spherical particles compared to the ample studies of settling spherical particles. Fornari *et al.* (2018) numerically studied the sedimentation of oblate spheroids with $\lambda = 1/3$ and $Ga = 60$ (corresponding to $Re_t = 38.7$) at different particle volume fraction by means of PR-DNS. It was demonstrated that the particle mean settling velocity is enhanced by at most 33% compared to the settling velocity of an isolated particle at $\phi = 0.5\%$. The substantial enhancement of particle settling speed is ascribed to the formation of particle clusters in the suspension. As for the case of prolate particles, to the best of the authors' knowledge, the only relevant study is Lu *et al.* (2023), who considered the settling of prolate particles with $\lambda = 2$ and $Ga = 41.8$ at $\phi = 2.2\%, 5.5\%$ and 9.9% in a relatively small periodic computational domain. They reported a decreased particle mean settling velocity, and a transition from hydrodynamic-interaction-dominated regime to particle-collision-dominated regime as ϕ increases.

1.3. *Objective of the present study*

According to the above literature review, we are still far from achieving a comprehensive understanding of the suspensions of settling non-spherical particles. There are a few unresolved key problems. For instance, how are non-spherical particles clustered and settling in dilute and dense suspensions? What are the governing mechanisms for the variation of non-spherical particle settling velocity at different volume fraction? What are the key factors influencing the collisions among settling non-spherical particles and how to quantify them? Motivated by these questions, we investigate the settling of a swarm of prolate spheroids in a quiescent fluid in this study. Our focus is on the effect of particle volume fraction on the settling velocity, clustering, microstructure, and collision rate of prolate particles. By means of PR-DNS, we simulate the settling prolate particles with an aspect ratio $\lambda = 3$, density ratio $\alpha = 2$, Galileo number $Ga = 80$ at different volume fractions. Different from previous studies (Uhlmann & Doychev 2014; Zaidi *et al.* 2014; Fornari *et al.* 2018), we start from a very low volume fraction at $\phi = 0.1\%$, and observe a non-monotonic variation of particle mean settling velocity from $\phi = 0.1\%$ to $\phi = 10\%$. Then, by carrying out the Voronoi analysis, we attribute the non-monotonic variation of $\langle V_s \rangle$ to the change of degree of particle clustering in the suspension. We also look into the microstructure of dispersed particles, and attribute the intense pair correlation at low particle volume fractions to the wake-flow-induced hydrodynamic interactions among settling particles. At last, we examine the collision efficiency of dispersed particles by computing the collision kernel in the system. We demonstrate that the decrease of collision kernel is primarily caused by the decrease of particle radial correlation as ϕ increases.

The remainder of this paper is organized as follows. In section 2, we describe the physical problem along with simulation set-ups of this study, and introduce the numerical methods adopted here. Then, in section 3, we analyze the statistics of particle motions and spatial distributions, and examine the collision efficiency of dispersed particles at different particle volume fraction. Finally, we summarize the findings and draw conclusions in section 4.

2. Simulation set-ups and numerical methods

2.1. *Flow configuration and physical parameters*

In the present work, we explore the gravitational sedimentation of prolate particles in a tri-periodic domain filled with an initially quiescent fluid, as shown in figure 1. The prolate particle with an aspect ratio $\lambda = a/b = 3$ and a density ratio $\alpha = \rho_p/\rho_f = 2$ (ρ_p and ρ_f represent the density of the particle and fluid, respectively) is considered here. The Galileo number defined by $Ga = \sqrt{(\alpha - 1)|\boldsymbol{g}|D_{eq}^3}/\nu$ is set as $Ga = 80$. Here, $D_{eq} = 2(ab^2)^{1/3}$

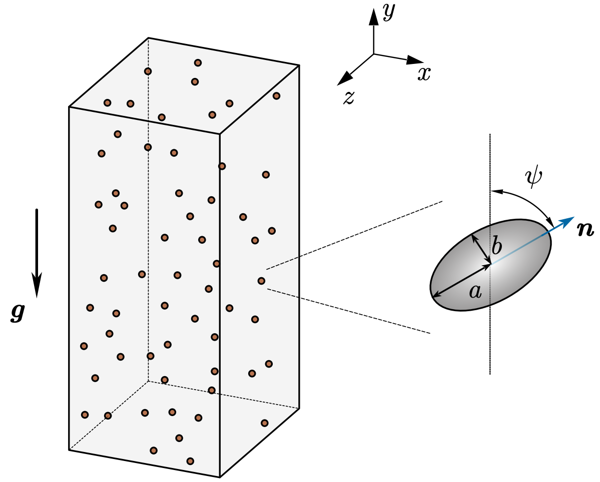

Figure 1: Schematic representation of settling prolate particles in a quiescent fluid. The semi-major and semi-minor axes of the prolate particle have a length of a and b, respectively. The unit vector along the symmetric axis of the prolate particle is denoted by $\boldsymbol{n}$. The angle between the vector $\boldsymbol{n}$ and the positive y direction is defined as the pitch angle ψ. The gravity is applied in the negative y direction with an acceleration of $\boldsymbol{g}$.

Case	ϕ	$\left[L_x \times L_y \times L_z\right]/D_{eq}^3$	N_p	N_{cell}
1	0.1%	$32 \times 100 \times 32$	196	1.416billion
2	0.5%	$32 \times 100 \times 32$	978	1.416billion
3	1%	$32 \times 100 \times 32$	1956	1.416billion
4	2%	$32 \times 100 \times 32$	3911	1.416billion
5	5%	$24 \times 60 \times 24$	3300	0.478billion
6	10%	$20 \times 50 \times 20$	3056	0.276billion

Table 1: Simulation set-ups for settling prolate particles with different particle volume fraction. N_{cell} denotes the number of grid cells used for the fluid flow simulation.

is the equivalent diameter of a sphere with the same volume of the prolate spheroid. In this study, we focus on the effect of particle volume fraction on the settling behavior of prolate particles. The particle volume fraction ϕ is defined by $\phi = (\pi N_p D_{eq}^3)/(6 L_x L_y L_z)$, in which N_p denotes the number of particles, and L_x, L_y and L_z represent the length of computational domain in x, y and z directions, respectively. As listed in table 1, we consider six simulation cases with different particle volume fractions. As the gravity is applied in the negative y direction, the computational domain along this vertical direction is set longer than the other two lateral directions. Note that for the cases with $\phi \geqslant 5\%$, we reduce the size of computational domain since the decorrelation of the fluid flows is more rapid with the increase of particle volume fraction (Zaidi *et al.* 2014; Zaidi 2018*b*). Initially, dispersed particles with random orientations are randomly seeded in the computational domain without overlaps (Anoukou *et al.* 2018). The statistics given in section 3 are obtained after the flow has reached a statistically steady state, which is ensured by monitoring the temporal evolution of particle mean settling velocity during the simulation.

2.2. *Flow simulation and immersed boundary method*

In the present work, we use the PR-DNS to solve the fluid flow laden with freely-moving particles. Specifically, we adopt the immersed boundary method (IBM) to resolve the particle-fluid interactions (Peskin 2002; Iaccarino & Mittal 2004). The fluid flow is governed by the incompressible Navier-Stokes (N-S) equations as:

$$\nabla \cdot \boldsymbol{u} = 0, \tag{2.1}$$

$$\rho_f \left(\frac{\partial \boldsymbol{u}}{\partial t} + \boldsymbol{u} \cdot \nabla \boldsymbol{u} \right) = -\nabla p + \mu \nabla^2 \boldsymbol{u} + \rho_f \boldsymbol{f}_{IB}. \tag{2.2}$$

Here, $\boldsymbol{u}$ and p represent the velocity and pressure of the fluid flow, respectively, and the fluid dynamic viscosity is denoted by μ. The forcing term $\boldsymbol{f}_{IB}$ in (2.2) represents the immersed boundary force (IB force) to satisfy the non-slip boundary condition on particle surfaces (as elaborated in the following).

To simulate the fluid flow, we employ a second-order finite difference method to numerically solve the N-S equations (2.1-2.2) (Kim *et al.* 2002). The temporal advancement from the nth to the $(n+1)$th time step using the Crank-Nicolson scheme is (Kim *et al.* 2002):

$$\frac{\boldsymbol{u}^* - \boldsymbol{u}^n}{\Delta t} + \frac{1}{2}\left(H(\boldsymbol{u}^*) + H(\boldsymbol{u}^n)\right) = -Gp^{n-1/2} + \frac{1}{2Re}\left(L\boldsymbol{u}^* + L\boldsymbol{u}^n\right), \tag{2.3}$$

$$\boldsymbol{u}^{**} = \boldsymbol{u}^* + \Delta t \boldsymbol{f}_{IB}^{n+1/2}, \tag{2.4}$$

$$DG\delta p = D\boldsymbol{u}^{**}/\Delta t, \tag{2.5}$$

$$p^{n+1/2} = p^{n-1/2} + \delta p, \tag{2.6}$$

$$\boldsymbol{u}^{n+1} = \boldsymbol{u}^{**} - \Delta t G\delta p. \tag{2.7}$$

Here, H, G, L and D represent the spatial discrete convection, gradient, Laplacian and divergence operators, respectively, which are calculated by the second-order central-difference scheme on a staggered Eulerian grid (Kim *et al.* 2002). In (2.3), the first prediction velocity $\boldsymbol{u}^*$ is updated without the consideration of IB forces. Then, the second prediction velocity $\boldsymbol{u}^{**}$ is calculated via (2.4) with the introduction of IB forces, which are evaluated as outlined in (2.8) - (2.10). Finally, the velocity projection step is performed, including the solution of the Poisson equation (2.5), and the update of pressure and fluid velocity to a new time step via (2.6) and (2.7). The parameter $Re = U_0 L_0/\nu$ presented in Eq. (2.3) is the Reynolds number based on the characteristic velocity (U_0) and length (L_0) to normalize the N-S equations (2.1-2.2).

In the implementation of IBM, the particle surface is represented by a set of Lagrangian marker points distributed on the particle surface. We adopt the method proposed by Eshghinejadfard *et al.* (2016) to allocate N_L Lagrangian marker points on the surface of each prolate spheroid. With regard to the calculation of IB forces presented in (2.4), we employ the direct-forcing IBM (Uhlmann 2005; Breugem 2012) as:

$$\boldsymbol{U}_l^* = \sum_{ijk} \boldsymbol{u}_{ijk}^* \delta\left(\boldsymbol{X}_l^n - \boldsymbol{x}_{ijk}\right) \Delta h^3, \tag{2.8}$$

$$\boldsymbol{F}_l^{n+1/2} = \frac{\boldsymbol{U}_p(\boldsymbol{X}_l^n) - \boldsymbol{U}_l^*}{\Delta t}, \tag{2.9}$$

$$\boldsymbol{f}_{IB,ijk}^{n+1/2} = \sum_{l} \boldsymbol{F}_l^{n+/2} \delta\left(\boldsymbol{x}_{ijk} - \boldsymbol{X}_l^n\right) \Delta V_l. \tag{2.10}$$

Here, the capital letters refer to the variables defined on the Lagrangian marker point. In (2.8), the first prediction velocity $\boldsymbol{u}^*$ is interpolated from the Eulerian grid to the Lagrangian

ε_Δ	ε_σ	$e_{n,d}$	$e_{t,d}$	μ_C	N
0.025	0.001	0.97	0.35	0.15	8

Table 2: Coefficients involved in the calculation of particle-particle collision force in (2.17), (2.20) and (2.21).

marker point using the Dirac-delta function $\delta(\cdot)$, in which $\boldsymbol{X}_l^n$ denotes the position of the lth Lagrangian marker point on the particle surface. Then, the IB force is calculated on the Lagrangian marker point through (2.9), where $\boldsymbol{U}_p$ represents the rigid velocity of the particle. Finally, the IB force is spread onto the Eulerian grid with the Dirac-delta function via (2.10), in which ΔV_l denotes the volume of the lth Lagrangian marker point. The Dirac-delta function used for the transformation of variables on the Eulerian grid and the Lagrangian point is defined by:

$$\delta\left(\boldsymbol{x}\right) = \frac{1}{\Delta h^3} \cdot \phi(\frac{x}{\Delta h}) \cdot \phi(\frac{y}{\Delta h}) \cdot \phi(\frac{z}{\Delta h}), \tag{2.11}$$

where $\phi(\cdot)$ is a 3-grid-width discrete Dirac-delta function as (Roma *et al.* 1999):

$$\phi(r) = \begin{cases} \frac{1}{6}(5 - 3|r| - \sqrt{-3(1-|r|)^2 + 1}), & 0.5 \leqslant |r| \leqslant 1.5 \\ \frac{1}{3}(1 + \sqrt{-3r^2 + 1}), & |r| \leqslant 0.5 \\ 0, & \text{otherwise.} \end{cases} \tag{2.12}$$

In the present simulations, the computational domain is discretized by a uniform Eulerian grid with a resolution of $\Delta h = \Delta x = \Delta y = \Delta z = D_{eq}/24$ (the total number of grid cells are listed in table 1). The total number of Lagrangian marker points to resolve the surface of one particle is $N_L = 2263$. This resolution has been verified to be fine enough for the simulation of particle settling motion (see Appendix A). Furthermore, as for the implementation of direct-forcing immersed boundary method, we adopt the multi-forcing scheme with $N_s = 2$ iterations to better approximate the non-slip boundary condition on the particle surface (Breugem 2012), and use the inward retraction of Lagrangian marker points with a distance of $r_d = 0.3\Delta h$ (Breugem 2012) to correct the excess in the particle effective diameter induced by the width of Dirac-delta function.

2.3. *Lagrangian tracking of particle motions*

The motion of dispersed particles in the fluid flow is governed by the Newton-Euler equations as follows:

$$\rho_p V_p \frac{d\boldsymbol{v}}{dt} = \boldsymbol{F}_H + \left(\rho_p - \rho_f\right) \boldsymbol{g} V_p + \boldsymbol{F}_C, \tag{2.13}$$

$$\frac{d(\boldsymbol{I} \cdot \boldsymbol{\omega})}{dt} = \boldsymbol{T}_H + \boldsymbol{T}_C. \tag{2.14}$$

Here, $\boldsymbol{v}$ and $\boldsymbol{\omega}$ denote the translational and rotational velocity of the particle, V_p and $\boldsymbol{I}$ represent the volume and the moment of inertia of the particle, respectively. In the present IBM simulation, the hydrodynamic force and torque acting on the particle, denoted by $\boldsymbol{F}_H$ and $\boldsymbol{T}_H$ in (2.13) and (2.14), respectively, are calculated by (Breugem 2012; Kempe &

Fröhlich 2012):

$$\boldsymbol{F}_H = -\rho_f \sum_l \boldsymbol{F}_l \Delta V_l + \rho_f \frac{d}{dt} \int_{V_p} \boldsymbol{u} dV, \tag{2.15}$$

$$\boldsymbol{T}_H = -\rho_f \sum_l \boldsymbol{r} \times \boldsymbol{F}_l \Delta V_l + \rho_f \frac{d}{dt} \int_{V_p} \boldsymbol{r} \times \boldsymbol{u} dV, \tag{2.16}$$

where $\boldsymbol{r} = \boldsymbol{x} - \boldsymbol{x}_C$ denotes the vector from the particle centroid to one point on the particle surface. Moreover, $\boldsymbol{F}_C$ and $\boldsymbol{T}_C$ in (2.13) and (2.14) denote the force and torque induced by particle-particle collisions. As for the collision model, we consider the sub-grid lubrication force correction when the surface-to-surface distance between two particles is smaller than one grid spacing, and apply the soft-sphere collision force to a pair of touching particles (Costa *et al.* 2015; Ardekani *et al.* 2016). Regarding the lubrication force, only the normal component (denoted by F_{Lub}) is considered and calculated by (Jeffrey 1982):

$$\frac{F_{Lub}}{-6\pi\mu R_p \Delta U_n} = \begin{cases} \lambda_{Lub}(\varepsilon) - \lambda_{Lub}(\varepsilon_\Delta), & \varepsilon_\sigma \leqslant \varepsilon < \varepsilon_\Delta \\ \lambda_{Lub}(\varepsilon_\sigma) - \lambda_{Lub}(\varepsilon_\Delta), & 0 \leqslant \varepsilon < \varepsilon_\sigma \\ 0. & otherwise \end{cases} \tag{2.17}$$

Here, R_p denotes the Gaussian radius of the prolate spheroid at the touching point; ΔU_n is the normal relative velocity between the touching points of two particles; ε is the normalized gap width between particle surfaces (normalized by R_p); λ_{Lub} is the Stokes amplification factor, which is a function of ε as (Jeffrey 1982):

$$\lambda_{Lub}(\varepsilon) = \frac{1}{4\varepsilon} - \frac{9}{40} \ln \varepsilon - \frac{3}{112} \varepsilon \ln \varepsilon + 0.6728. \tag{2.18}$$

Additionally, ε_Δ in (2.17) is the cut-off gap width to activate of the lubrication correction, and ε_σ is a threshold related to the particle surface roughness, below which the lubrication force becomes saturated (Costa *et al.* 2015). The values of these two coefficients adopted in the present work are listed in table 2.

With regard to the soft-sphere collision force, we employ the spring-dashpot-slide model to address the collision between contacting particles (Costa *et al.* 2015; Ardekani *et al.* 2016). In this model, the normal and tangential components of the collision force are expressed as (Costa *et al.* 2015):

$$F_n = -k_n \delta_n - \eta_n \Delta U_n, \tag{2.19}$$

$$F_t = \min\left(\|-k_t \delta_t - \eta_t \Delta U_t\|, \|-\mu_c F_n\|\right), \tag{2.20}$$

where δ_n represents the overlap between the two contacting particles, δ_t is the tangential displacement, and ΔU_t denotes the tangential component of the relative velocity of the contacting points. The spring and dashpot coefficients in (2.19) and (2.20) are given by (Costa *et al.* 2015):

$$\begin{aligned} k_n &= \frac{m_e(\pi^2 + \ln^2 e_{n,d})}{(N\Delta t)^2}, \quad \eta_n = -\frac{2m_e \ln e_{n,d}}{N\Delta t}, \\ k_t &= \frac{m_{e,t}(\pi^2 + \ln^2 e_{t,d})}{(N\Delta t)^2}, \quad \eta_t = -\frac{2m_{e,t} \ln e_{t,d}}{N\Delta t}, \end{aligned} \tag{2.21}$$

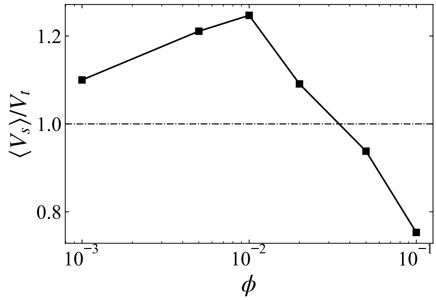

Figure 2: Mean settling velocity of particles at different volume fraction.

where

$$\begin{aligned} m_e &= \left(m_i^{-1} + m_j^{-1}\right)^{-1}, \\ m_{e,t} &= \left(1 + 1/K^2\right)^{-1} m_e, \end{aligned} \tag{2.22}$$

with m_i, m_j being the mass of the two colliding particles and $K = \sqrt{2/5}$ being the normalized radius of gyration for the approximating sphere. The motivation of formulating the spring and dashpot coefficients as (2.21) is to define the collision time as a multiple N of the time step Δt (Costa *et al.* 2015). The parameter N, the restitution coefficients $e_{n,d}$ and $e_{t,d}$ in (2.21), and the sliding friction μ_c in (2.20) adopted in the present work are provided in table 2. More details and validations about the particle-particle collision model can be found in Costa *et al.* (2015) and Ardekani *et al.* (2016). In addition, after obtaining the collision force $\boldsymbol{F}_C$, the collision torque is calculated by $\boldsymbol{T}_C = \boldsymbol{R}_C \times \boldsymbol{F}_C$, in which $\boldsymbol{R}_C$ represents the vector from the particle centroid to the collision point.

In Appendix A, we provide a validation of the present numerical method by simulating the DKT of two settling spheres. In addition, we carry out the grid dependence test to justify the grid resolution adopted in this study by simulating the settling motion of an isolated prolate spheroid in Appendix A.

3. Results and discussion

3.1. *Mean settling velocity of particles*

First of all, we look into the mean settling velocity of dispersed particles. Here, the settling velocity is defined as the component of particle velocity along the gravitational direction, i.e. $V_s = \boldsymbol{v} \cdot \boldsymbol{e}_g$. As shown in figure 2, the mean settling velocity, denoted by $\langle V_s \rangle$, exhibits a non-monotonic variation with the increase of particle volume fraction from $\phi = 0.1\%$ to $\phi = 10\%$. Specifically, the mean settling velocity is greater than the settling velocity of an isolated particle when $\phi \leqslant 2\%$, with a peak value of $\langle V_s \rangle \approx 1.25 V_t$ at $\phi = 1\%$, and decreases to less than V_t when the particle volume fraction exceeds 5%. In the following parts, we examine the orientation and the spatial distribution of dispersed particles, to uncover the physics of the non-monotonic variation of mean settling velocity with the change of volume fraction.

3.1.1. *Effect of particle orientation*

Different from the spherical particle, it is known that a prolate particle experiences a smaller drag and settles faster when its major axis tend to align with the gravitational direction. Therefore, the particle orientation is essential in the settling behavior of non-spherical

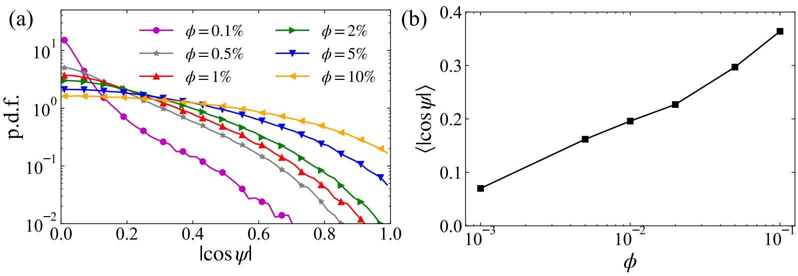

Figure 3: (a) P.d.f. of the cosine value of the pitch angle ψ at different volume fraction. (b) Mean value of $|\cos\psi|$ as a function of particle volume fraction.

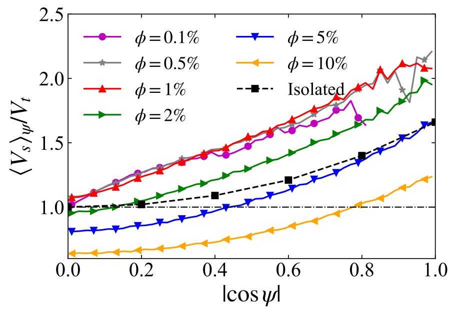

Figure 4: Conditionally averaged settling velocity versus particle orientation. The dashed line labelled by "Isolated" represents the isolated prolate particle settling with an artificial fixed pitch angle.

particles. One may ask whether the variation of particle mean settling velocity is caused by the change of particle orientation distribution. To verify this conjecture, we first investigate the statistics of particle orientations in the suspension with different volume fraction. In figure 3 (a), we provide the probability density function (p.d.f.) of the cosine value of the particle pitch angle ψ. We observe that the preference of broad-side-on orientation ($\psi = 90°$, which is the steady orientation of the isolated settling prolate particle) becomes less pronounced with the increase of particle volume fraction. Instead, the orientation of dispersed particles progressively approaches a random distribution at a higher ϕ. This change is also manifested by the increase of the mean value of $|\cos\psi|$ as ϕ increases as shown in figure 3 (b). This observation is in qualitative agreement with the previous study of settling oblate particles (Fornari *et al.* 2018). Hence, we can infer that the disturbances from hydrodynamic interactions and particle-particle collisions, which randomize particle orientations, are enhanced as the particle volume fraction grows.

Furthermore, we examine the correlation between particle orientation and settling velocity. We present the conditionally averaged settling velocity with respect to the particle pitch angle (denoted by $\langle V_s\rangle_\psi$) in figure 4. For comparison, we also conduct a group of simulations of the isolate settling prolate spheroid with artificially fixed pitch angles. It is observed that with the increase of $|\cos\psi|$ from 0 to 1, $\langle V_s\rangle_\psi$ increases monotonically, regardless of particle volume fraction, just as the single prolate spheroid does. This result, together with what is shown in figure 3, can partially interpret the increase of particle mean settling velocity from $\phi = 0.1\%$ to $\phi = 1\%$, since more particles settle with the orientation closer to $|\cos\psi| = 1$ as ϕ increases. Nevertheless, the mean settling velocity of particles does not increase monotonically in accordance with the increasing trend of $\langle|\cos\psi|\rangle$ for $\phi > 1\%$. Therefore, the modulation of

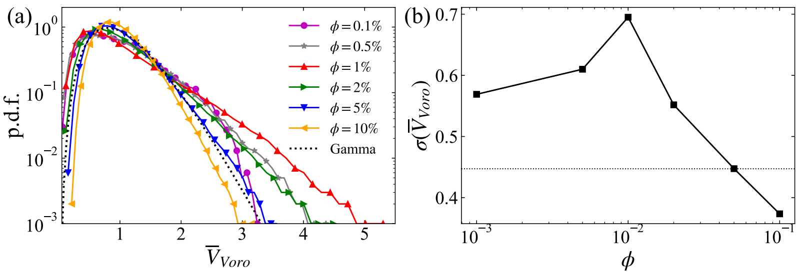

Figure 5: Voronoi analysis of the spatial distribution of dispersed particles at different particle volume fraction. (a) P.d.f. of the normalized volume of Voronoi tessellations. (b) The standard deviation of Voronoi volumes as a function of ϕ. The dotted line represents the result of a Gamma distribution with $\sigma(\overline{V}_{Voro}) = 0.447$.

particle orientation is not the dominant factor to affect the mean settling velocity of prolate spheroids.

3.1.2. *Effect of particle clustering*

Previous studies found that particle clustering can substantially enhance the mean settling velocity of particles (Kajishima 2004; Uhlmann & Doychev 2014; Fornari *et al.* 2018). Therefore, we examine the spatial distribution of dispersed particles in this section using the Voronoi analysis (Monchaux *et al.* 2010). Specifically, the entire computational domain is partitioned into N_p cells, i.e. Voronoi tessellations. The partitioning rule ensures that a point in the ith tessellation is closer to the centroid of the ith particle than any other particle. In this manner, the spatial distribution of dispersed particles can be quantified by the statistics of the normalized volume of Voronoi tessellations, namely $\overline{V}_{Voro}(i) = V_{Voro}(i)N_p/V_{tot}$, where $V_{Voro}(i)$ is the volume of the ith Voronoi tessellation, and V_{tot} is volume of the whole domain. If the dispersed particles are orderly distributed in the space (like molecules in a crystal), the whole domain is evenly partitioned so that $\overline{V}_{Voro} \equiv 1$ and the standard deviation is $\sigma(\overline{V}_{Voro}) = 0$. While, if particles are randomly scattered in the space, the statistics of $\overline{V}_{Voro}$ subject to a Gamma distribution with a standard deviation $\sigma(\overline{V}_{Voro}) = 0.447$ (Ferenc & Néda 2007). Moreover, if dispersed particles preferentially accumulate in some specific regions, the prevalence of particle clusters (represented by small values of $\overline{V}_{Voro}$) and voids (represented by large values of $\overline{V}_{Voro}$) would flatten the p.d.f. of $\overline{V}_{Voro}$ and thus increases the standard deviation $\sigma(\overline{V}_{Voro})$ (Monchaux *et al.* 2010).

Figure 5 illustrates the results of the Voronoi analysis at different volume fraction. The p.d.f. of $\overline{V}_{Voro}$ exhibits a pronounced higher tail in relative dilute suspensions with $0.5\% \leqslant \phi \leqslant 2\%$, and becomes narrower than the Gamma distribution at $\phi = 10\%$. Additionally, the standard deviation of $\overline{V}_{Voro}$, as depicted in figure 5 (b), exhibits a non-monotonic variation with the increase of ϕ, with a value greater than that of the Gamma distribution in the cases with $\phi \leqslant 2\%$ and less than it at $\phi = 10\%$. This indicates that the tendency of dispersed particles to form clusters is initially intensified as ϕ grows at $\phi \leqslant 1\%$, but is then attenuated at higher volume fraction. It is noteworthy that the non-monotonic variation of $\sigma(\overline{V}_{Voro})$ is strikingly similar to the variation of particle mean settling velocity (see figure 2). Therefore, the degree of particle clustering quantified by $\sigma(\overline{V}_{Voro})$ is highly correlated with the particle mean settling velocity in this flow system. We elaborate on this correlation in the following paragraphs.

First, we compute the conditionally averaged settling velocity with respect to the Voronoi volume (denoted by $\langle V_s \rangle_{V_{Voro}}$). As shown in figure 6, the particles with a small Voronoi

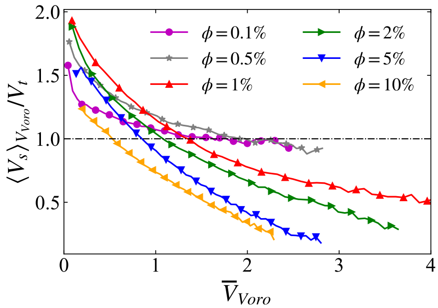

Figure 6: Conditionally averaged settling velocity versus the Voronoi volume at different volume fraction.

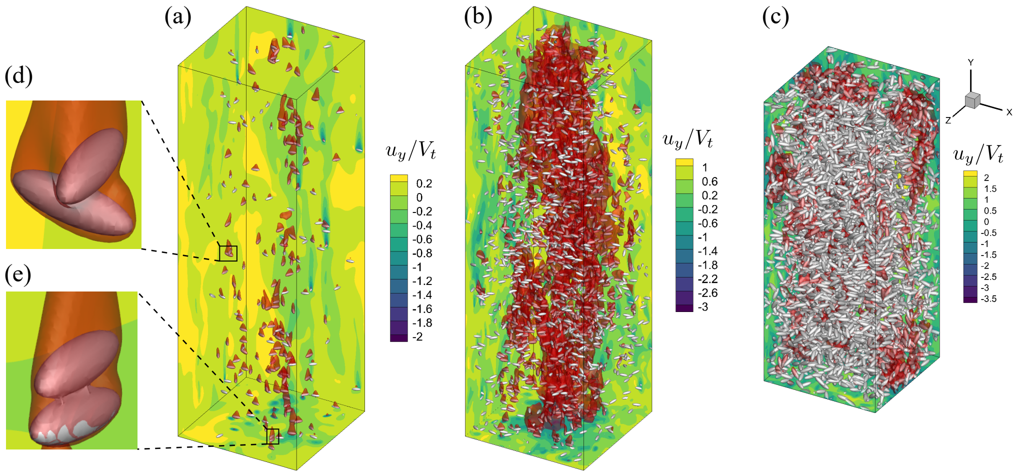

Figure 7: Snapshots of instantaneous three-dimensional flow field at (a) $\phi = 0.1\%$, (b) $\phi = 1\%$ and (c) $\phi = 10\%$. (d), (e) Zoom-in view of (a) to illustrate touching particle pairs at $\phi = 0.1\%$. The dispersed prolate particles are depicted in grey. The vertical velocity of $u_y = -V_t$ are represented by red iso-surfaces.

cell tend to settle faster, regardless of particle volume fraction. This phenomenon can be explained by the so-called "swarm effect" (Koch & Hill 2001; Wang *et al.* 2022), which suggests that a cluster of settling particles experiences a lower total drag than the sum of drag of individual particles of the same number. In contrast, when particles are located in the regions devoid of particles (corresponding to large values of V_{Voro}), the settling motion is hindered since more intense upward flows in these regions exert a greater hydrodynamic drag on the involved particles.

In the previous studies of settling spherical particles (Kajishima 2004; Zaidi *et al.* 2014) and settling oblate particles (Fornari *et al.* 2018; Moriche *et al.* 2023), the DKT interactions have been regarded as the major mechanism leading to the formation of particle clusters in the multi-settling-particle system. Specifically, the attraction by the wake flow reduces the distance among settling particles. If two particles undergoing a DKT process can further attract other particles before they separate, the number of accumulated particles grows progressively, and eventually form large-scale particle clusters in the system (Moriche *et al.* 2023). Also, it has been demonstrated by Ardekani *et al.* (2016) that the interaction time is longer and the attraction zone is larger for the DKT process of a pair of non-spherical particles than spherical ones. This explains why the clustering of prolate particles can be observed in

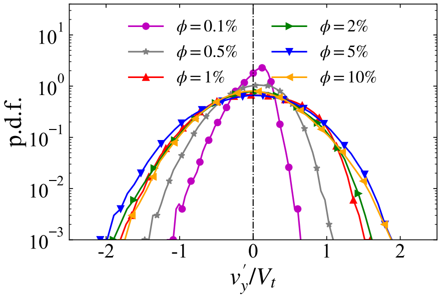

Figure 8: P.d.f. of the particle velocity fluctuations in the vertical direction.

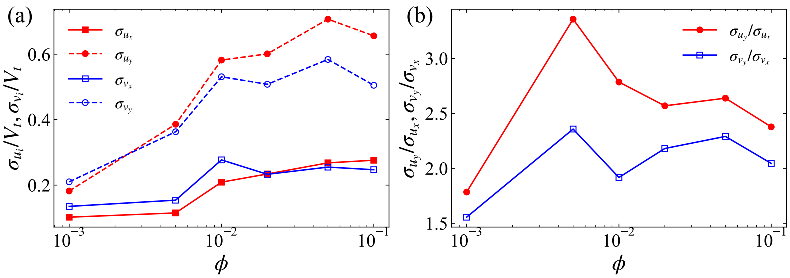

Figure 9: (a) Standard deviation of particle and fluid velocity in the vertical (denoted by the subscript 'y') and horizontal direction (denoted by the subscript 'x'). (b) The ratio between the standard deviation of vertical and horizontal velocity components for the fluid and particle phase.

the present study, similar to the case of oblate particles (Fornari *et al.* 2018; Moriche *et al.* 2023), although spherical particles cannot form clusters at a comparable Reynolds number and volume fraction (Zaidi *et al.* 2014).

To further show the different level of particle clustering at different volume fraction, we present the visualization of flow field at $\phi = 0.1\%$, 1% and 10% in figure 7. In the case with the most intense particle clustering ($\phi = 1\%$ case in figure 7 (b)), we observe a very-large-scale flow structure, manifested by a connection of particle wakes wriggling along the vertical direction. This flow structure is the footprint of the column-like particle clusters whose scale is as large as the whole computational domain (Moriche *et al.* 2023). However, in the case of lowest particle volume fraction under consideration ($\phi = 0.1\%$ case as shown in figure 7 (a)), the tendency of particle clustering is weakened. Recalling the mechanism of the formation of particle clusters, we attribute the absence of large-scale particle clusters to the too large inter-particle distance in this scenario. Although the attraction between pairwise particles by wake flows still takes place in this case (see discussions in section 3.2), the continuous attraction of particles to cause particle clustering becomes infrequent for the long particle-particle distance. While, in another limit with a high volume fraction at $\phi = 10\%$, the dispersed particles are crowded in the suspension as illustrated in figure 7 (c). As a result, the small particle-particle distance disrupts wake flows of settling particles, so as to inhibit the occurrence of particle clustering.

Furthermore, we look into the fluctuations of particle velocity at different volume fraction. First, as depicted in figure 8, the p.d.f. of particle vertical velocity fluctuation is skewed with a higher negative tail at low volume fractions. This observation, which is most pronounced at $\phi = 0.1\%$, indicates that particles tend to preferentially sample the downward flows. In other words, particles are likely to be attracted and entrapped in wake flows. These hydrodynamic interactions, however, are weakened as the particle volume grows, manifested by the recovery of the p.d.f. of v'_y to the symmetric shape. Moreover, we provide the standard deviation of the particle and fluid velocity at different volume fraction in figure 9 (a). In principle, the magnitude of particle and fluid velocity fluctuation increases with the addition of more particles in the suspension. While, a local rise of the particle velocity fluctuation occurs at $\phi = 1\%$, which may be related to the enhanced particle-particle interactions in large-scale particle clusters. In addition, both of particle and fluid velocity fluctuations are anisotropic with a higher standard deviation in the vertical direction. As depicted in figure 9 (b), the ratio between the vertical and horizontal velocity fluctuation is higher for the fluid than that of particles in all cases.

In a brief summary of this section, hydrodynamic interactions play an important role in the spatial distribution and mean settling velocity of dispersed particles. In very dilute suspensions, although large-scale particle clusters do not form due to the long distance among particles, the wake-flow-induced attraction still works, by which particles preferentially sampling downward wake flows settle faster. This mechanism explains the considerable enhancement of $\langle V_s \rangle$ by approximately 10% comparing to V_t when the particle volume fraction is as low as $\phi = 0.1\%$. Then, with the increase of particle volume fraction, frequent attractions among particles cause the growth of particle clusters to a large size. The particle clustering is most significant at $\phi = 1\%$, resulting in a substantial enhancement of particle mean settling velocity by around 25%. However, in the denser suspensions with the volume fraction $\phi \geqslant 5\%$, the particle clustering is inhibited, since the dispersed particles are so crowded to disrupt particle wakes. In this regime, hindrance effect becomes predominant, and reduces the mean settling velocity to less than the isolated settling velocity. In contrast, the change of particle orientation is not the determining factor to influence the mean settling velocity, although individual prolate spheroids still tend to settle faster when the orientation deviates more from the broad-side-on alignment in suspensions.

3.2. *Microstructures of dispersed particles*

According to the above discussion, settling particles are spatially clustered depending on the particle volume fraction. Therefore, it is of interest to examine the particle microstructures. First, we calculate the pair distribution function $P(\boldsymbol{r})$, which provides the information about the probability to find another particle relative to a reference particle with a separation vector $\boldsymbol{r}$. The definition of $P(\boldsymbol{r})$ is referred to Yin & Koch (2007), Zaidi *et al.* (2015) and Fornari *et al.* (2018). By definition, $P(\boldsymbol{r}) > 1$ indicates a higher probability of finding a pair of particles with a separation of $\boldsymbol{r}$ compared to the nominally random distribution of particles. In addition, as $P(\boldsymbol{r})$ is axisymmetric about the direction of gravity, we calculate the average of $P(\boldsymbol{r})$ over the azimuth angle θ (the angle between the positive x direction and the projection of $\boldsymbol{r}$ onto the horizontal plane), and obtain the pair distribution function as a function of the separation distance $r = \|\boldsymbol{r}\|$ and the polar angle φ (the angle between the positive y direction and the vector $\boldsymbol{r}$), i.e.:

$$P(r,\varphi) = \frac{1}{2\pi}\int_0^{2\pi} P(\boldsymbol{r})\, d\theta = \frac{1}{2\pi}\int_0^{2\pi} P(r,\theta,\varphi)\, d\theta. \tag{3.1}$$

Figure 10 shows the pair distribution function at different volume fraction. We observe that the value of $P(r,\varphi)$ is significantly greater than unity along the vertical direction in dilute suspensions, which indicates that dispersed particles prefer to form vertically column-like structures, which is attributed to the hydrodynamic attraction of trailing particles to wake regions of leading particles. However, regarding the suspensions of settling spherical particles with similar configurations ($Re_t < 50$ and $\phi \approx 1\%$), nearby particles tend to repel

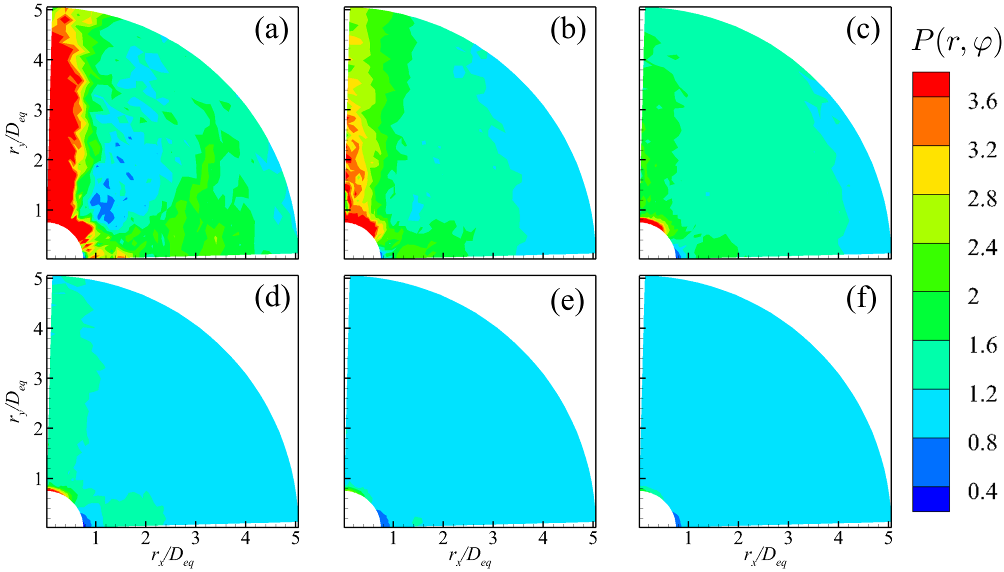

Figure 10: Pair distribution function of particles at different volume fraction. (a) ϕ = 0.1%; (b) ϕ = 0.5%; (c) ϕ = 1%; (d) ϕ = 2%; (e) ϕ = 5%; (f) ϕ = 10%. Here, the horizontal and vertical directions are denoted by $r_x = r \sin\varphi$ and $r_y = r\cos\varphi$, respectively.

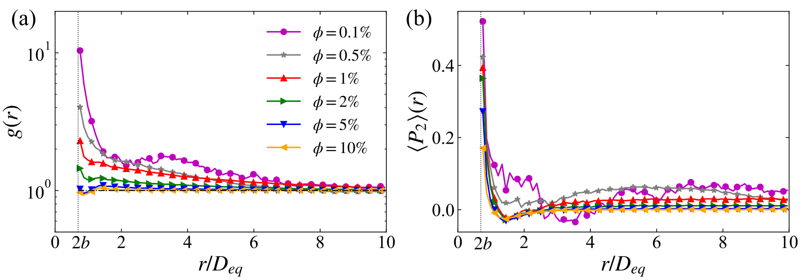

Figure 11: (a) Radial distribution function and (b) order parameter of particle pairs as the function of separation distance r.

each other and form particle deficit at small-distance separations (Yin & Koch 2007; Zaidi 2018*b*). The difference of microstructures between spherical and prolate particles reflects the shape-dependency of wake-flow-induced hydrodynamic interactions. Regarding prolate spheroids, the attraction and entrapment of the wake flow are strong to make particles to reside in wake regions (Ardekani *et al.* 2016). However, as for spherical particles, the lift force due to the shear flow is dominant in wake flows, and pushes the trailing particle outsides the wake region (Yin & Koch 2007). While, with the increase of particle volume fraction, the column-like microstructure is gradually attenuated (even in the case of ϕ = 1% where the particle clustering is the most intense), and eventually becomes negligible at $\phi \geqslant 5\%$.

Moreover, we quantify the radial and angular characteristics of particle microstructures by providing the radial distribution function (RDF) and the order parameter of particle pair statistics. On the one hand, the RDF, denoted by $g(r)$, is calculated from the two-dimensional

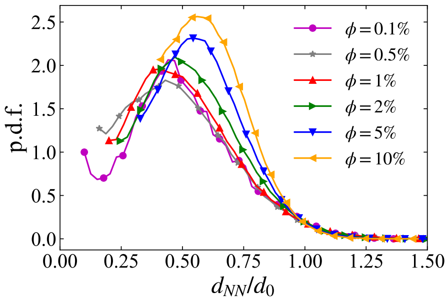

Figure 12: P.d.f. of the normalized NND at different volume fraction. Each line starts from $d_{NN} = 2b$, which is the theoretically smallest center-to-center distance between two particles with consideration of the particle finite-size.

pair distribution $P(r,\varphi)$ by (Yin & Koch 2007):

$$g\left(r\right)=\frac{1}{2}\int_{0}^{\pi}P\left(r,\varphi\right)\sin\varphi d\varphi. \tag{3.2}$$

As shown in figure 11 (a), the correlation of particle distribution is considerable enhanced with $g(r)>1$ for small separation distance r in dilute suspensions. The peak value of $g(r)$, which is evaluated at the separation distance $r=2b$ for $\phi\leqslant 2\%$, decreases monotonically with the increase of particle volume fraction. While, as the separation distance r grows, the RDF gradually decays to $g(r)\sim 1$, indicating the recovery to the random distribution for particle pairs with long-distance separations. While, in dense suspensions of $\phi=5\%$ and $\phi=10\%$, the RDF is close to one for all separation distance, indicating the weakening of microstructures in these cases.

On the other hand, the order parameter $\langle P_2\rangle(r)$, which quantifies the preferential orientation of particle pairs, is defined as the angular average of the second Legendre polynomial (Yin & Koch 2007; Fornari *et al.* 2018):

$$\left\langle P_2\right\rangle\left(r\right)=\frac{\int_0^{\pi}P(r,\varphi)P_2(\cos\varphi)\sin\varphi\mathrm{d}\varphi}{\int_0^{\pi}P(r,\varphi)\sin\varphi\mathrm{d}\varphi}, \tag{3.3}$$

in which $P_2\left(\cos\varphi\right)=\left(3\cos^2\varphi-1\right)/2$. The value of $\langle P_2\rangle(r)$ is equal to 1 for the case of all particle pairs with separation r aligning vertically, 0 for the isotropic arrangement, and -1/2 if the particle pairs are horizontally aligned (Yin & Koch 2007). In figure 11 (b), we depict the order parameter as the function of radial separation distance r at different volume fraction. In all cases under consideration, the order parameter is greater than zero at $r=2b$, indicating the tendency of nearby particle pairs to align vertically. This observation also manifests the hydrodynamic interactions induced by particle wakes in the present system. While, with the growth of particle volume fraction, the peak value of $\langle P_2\rangle$ is reduced, which is in agreement with the attenuation of particle microstructures in dense suspensions as shown in figure 10. Additionally, $\langle P_2\rangle(r)$ decays to zero rapidly with the increase of separation distance r in the suspensions with $\phi\geqslant 2\%$, indicating the recovery to an isotropic particle distribution. However, in the cases with lower volume fractions, the order parameter does not converge to zero with a slightly positive value even for long-distance particle separation of $r\sim 10D_{eq}$, which indicates that the wake-flow-induced hydrodynamic interactions have a long working distance in dilute suspensions.

In the previous studies of settling particles, the degree of particle clustering is usually quantified by the maximum value of RDF (Zaidi *et al.* 2014; Fornari *et al.* 2018; Zaidi

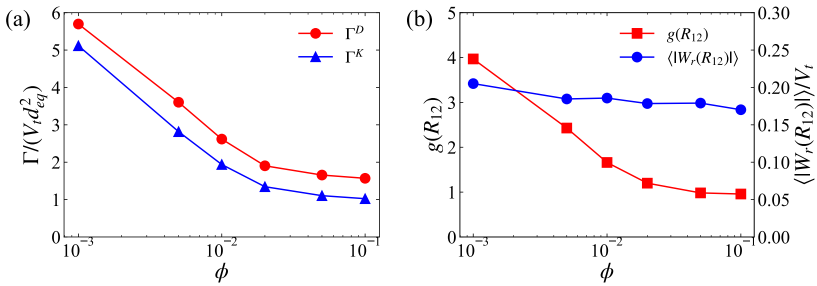

Figure 13: (a) Dynamic and kinematic collision kernels and (b) the RDF and RRV of dispersed particles at different particle volume fraction.

2018*a*). However, in the present work, we find that the monotonic decrease of the maximum value of $g(r)$ (see figure 11 (a)) does not agree with the non-monotonic variation of particle clustering, as quantified by the standard deviation of the normalized Voronoi volume (see figure 5 (b)). The inconsistency primarily exists in the very dilute suspensions with $\phi < 1\%$. To interpret this inconsistency, we further look into the statistics of the nearest neighbor distance (NND) of particles. NND of the ith particle is defined as (Zaidi *et al.* 2014):

$$d_{NN}(i) = \min_{j=1,2,\ldots,N_p, j\neq i} \left\| \boldsymbol{x}_i - \boldsymbol{x}_j \right\|, \tag{3.4}$$

where $\boldsymbol{x}_i$ denotes the position of the ith particle. In figure 12, we illustrate the p.d.f. of the normalized NND, namely d_{NN}/d_0, in each case under consideration. Here, we use $d_0(\phi) = (\pi/6)^{-1/3}\phi^{-1/3}D_{eq}$, which is the particle-particle distance for a cubic-lattice arrangement of particles with the volume fraction ϕ, to normalize the NND. Accordingly, we define a characteristic NND in the system, denoted by d^*_{NN}, as the value of d_{NN} corresponding to the peak of the p.d.f. of the normalized NND. As shown in figure 12, the value of d^*_{NN}/d_0 is smallest at $\phi = 1\%$, corresponding to the most significant particle clustering among all cases, and shifts to larger values in suspensions with both lower or higher ϕ. In fact, the small value of d^*_{NN}/d_0 manifests the compact arrangement of dispersed particles, and is an indicator of particle clustering. Moreover, note that there is an evident secondary peak of the p.d.f. of the normalized NND (evaluated at $d_{NN} = 2b$) in the very dilute suspension at $\phi = 0.1\%$ (it can also be observed at $\phi = 0.5\%$ but less pronounced). We attribute the presence of this secondary peak to the pairwise close-distance settling particles undergoing the kissing stage of the DKT process (see figure 7 (d-e)). This behavior, rather than particle clustering, can also interpret the large value of $g(r)$ at $r = 2b$ in very dilute suspensions. With the increase of particle volume fraction, the hydrodynamic disturbances and inter-particle collisions become more intense and frequent. The touching particle pairs may become less stable under the action of these disturbances, resulting in the disappearance of the secondary peak of the p.d.f. of NND at $d_{NN} = 2b$.

In summary, the standard deviation of the normalized Voronoi volume, instead of the maximum value of the RDF, should be regarded as a rational indicator to quantify the degree of particle clustering and to predict the mean settling velocity of particles.

3.3. *Particle-particle collisions*

The collision rate among dispersed particles is relevant in many practical applications, and affected by the particle spatial distribution (Wang *et al.* 2005). Therefore, we then examine the collision rate of settling particles in the present flow system. Here, we use the collision kernel Γ to quantify the collision efficiency of dispersed particles. The dynamic collision kernel, denoted by Γ^D, is defined by (Wang *et al.* 2000, 2005):

$$\Gamma^D = \frac{2\dot{N}_C}{n^2}, \tag{3.5}$$

where $\dot{N}_C$ represents the averaged number of collision events per unit volume per unit time, and $n = N_p/V_{tot}$ is the number density of the particles in the suspension. In the meantime, the collision kernel can also be regarded as the inward flux of particles across the surface of a collision sphere with a collision radius R_{12}. Accordingly, the kinematic collision kernel, denoted by Γ^K, can be defined as (Wang *et al.* 2000, 2005):

$$\Gamma^K = 2\pi R_{12}^2 \left\langle \left| W_r \left(R_{12} \right) \right| \right\rangle g \left(R_{12} \right). \tag{3.6}$$

Here, $\langle |W_r(R_{12})| \rangle$ represents the average radial relative velocity (RRV) of particles with a center-to-center distance R_{12}, and $g(R_{12})$ is the radial distribution function at the collision radius R_{12}. For spherical particles, Γ^K is strictly equivalent to Γ^D with the collision radius being the diameter of the sphere (Wang *et al.* 2000). However, regarding spheroidal particles, deriving the exact formulation of the kinematic collision kernel Γ^K is theoretically challenging due to the complexity of particle geometry. Alternatively, Siewert *et al.* (2014) suggested using the expression (3.6) as an approximate kinematic collision kernel for spheroidal particles, in which the equivalent diameter of the spheroid is used as the collision radius (i.e. $R_{12} = D_{eq}$).

In figure 13 (a), we illustrate the dynamic and approximate kinematic collision kernel of settling prolate particles at different volume fraction. The comparison between Γ^K and Γ^D reveals that the approximate kinematic collision kernel underestimates the exact dynamic collision kernel in the present flow system. Even though, Γ^K still provides a reasonable estimation of the collision kernel since it qualitatively captures the decreasing trend of Γ^D with the increase of ϕ. Furthermore, contributions to the kinematic collision kernel Γ^K, namely the RRV and RDF of the dispersed particles, are provided in figure 13 (b). We observe that the mean RRV exhibits a minor degree of variation with the change of volume fraction. This observation is different from the enhancement of RRV among settling spheroidal particles (with neglecting particle-particle interactions) in the homogeneous isotropic turbulence (Siewert *et al.* 2014; Jucha *et al.* 2018). The increased RRV of particles in the turbulent flow was ascribed to the dispersed settling velocity of spheroidal particles with random orientations (Siewert *et al.* 2014). However, this mechanism does not apply in the present flow system, as the RRV of particles is almost not changed even though the particle orientation becomes more random with the increase of volume fraction (see figure 3 (b)). In contrast, figure 13 (b) demonstrates that the decrease of $g(R_{12})$ makes a significant contribution to the decrease of collision kernel as ϕ grows.

Thus, in our point of view, hydrodynamic interactions play an significant role in the collision efficiency of dispersed particles through two mechanisms. First, the lubrication effect between approaching/separating particles determines the mean RRV of colliding particles. This mechanism is particle-volume-fraction independent since it applies to nearby particles, and results in an almost constant value of $\langle |W_r(R_{12})| \rangle$ at different ϕ. Second, the wake-flow-induced hydrodynamic interactions lead to the increase of RDF at low particle volume fractions (as discussed in section 3.2). Hence, the greatest radial correlation of particle pairs in the very dilute suspension at $\phi = 0.1\%$ (see figure 11 (a)) gives rise to the largest collision kernel among all cases of the present study. Accordingly, we remark that although the maximum value of RDF is not an appropriate criterion to quantify the particle clustering, the radial distribution function is especially relevant to the collision efficiency of settling particles by directly contributing to the kinematic collision kernel.

4. Concluding remarks

In the present work, we investigate the settling of prolate particles in a quiescent fluid by means of PR-DNS. With a focus on the volume fraction effect, we find a non-monotonic variation of particle mean settling velocity with the increase of particle volume fraction from $\phi = 0.1\%$ to $\phi = 10\%$. The highest mean settling velocity is observed at an intermediate volume fraction at $\phi = 1\%$, which is accompanied by the most significant particle clustering. We find that the swarm effect reduces the hydrodynamic drag acting on the clustered particles, which interprets the enhanced settling rate of particles. While, at lower particle volume fractions, the degree of particle clustering is attenuated, as the particle-particle distance is too large to for large-scale particle clusters. However, particles still tend to be attracted into the downward wake flows, which is manifested by the skewed distribution of particle vertical velocity fluctuations. This wake-flow-induced hydrodynamic interaction can also explain the considerable increase of mean settling velocity in the very dilute case of $\phi = 0.1\%$. In the case of high volume fraction, the crowded arrangement of particles disrupts the wakes behind particles, and inhibits the formation of particle clusters. As a result, hindrance effect dominates, leading to a reduction of mean settling velocity.

By performing the Voronoi analysis of the spatial distribution of particles, we find that the standard deviation of the normalized Voronoi volume can be regarded as an indicator to quantify the degree of particle clustering. On the one hand, with the increase of particle volume fraction, this quantity exhibits a strikingly similar non-monotonic variation as the particle mean settling velocity does. On the other hand, we observe a correlation between the particle settling velocity and the normalized Voronoi volume, which confirms the aforementioned swarm effect. In contrast, the change of particle orientation is not the determining factor to influence the mean settling velocity of particles. Although individual prolate spheroids still tend to settle faster when the particle orientation deviates more from the broad-side-on orientation in suspensions, the mean settling velocity does not increase in accordance with the monotonic increase of $|\cos\psi|$ at higher ϕ.

Moreover, we also investigate the microstructure of particles by analyzing particle pair statistics. By calculating the pair distribution function, we demonstrate that the probability to find vertically aligned particle pairs is substantially increased in dilute suspensions. The enhanced particle pair correlation reflects the strong effect of attraction and entrapment of prolate particles in wake flow regions, which is progressively attenuated with the growth of particle volume fraction. Furthermore, we examine the statistics of the nearest neighboring distance of dispersed particles. The smallest value of the normalized characteristic NND at $\phi = 1\%$ confirms again the highest degree of particle clustering in this case. Additionally, the secondary peak of the p.d.f. of NND observed in very dilute suspensions reflects the prevalence of touching particle pairs caused by wake-flow-induced attractions. This behavior can also interpret the substantially great value of the maximum of RDF at $\phi = 0.1\%$, although the particle clustering is less pronounced. Accordingly, we conclude that the maximum value of RDF is not an appropriate indicator to quantify the degree of particle clustering in the present flow system.

The final part of our study focuses on the collision of settling particles. The collision efficiency, which is quantified by the collision kernel, decreases monotonically with the increase of particle volume fraction. By examining the two contributions to the kinematic collision kernel, we demonstrate that the decrease of collision kernel as ϕ grows is primarily caused by the decrease of RDF, which is related to the microstructure of dispersed particles as discussed above. On the contrary, the radial relative velocity between colliding particles is almost a constant with the change of particle volume fraction. We attribute these results to

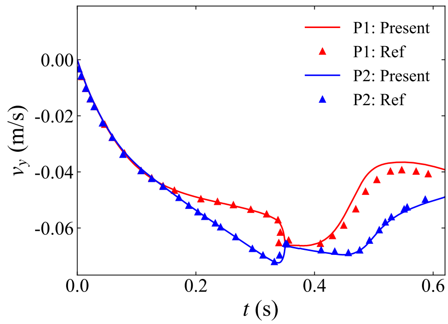

Figure 14: Time evolution of the vertical velocity of two settling spheres undergoing the DKT interaction. P1 and P2 denote the initially leading and trailing particle, respectively. "Ref" represents the result reported in the reference (Breugem 2012).

the essential influence of hydrodynamic interactions, including the wake-flow-induced effect and the lubrication effect of nearby particles, on the collision of settling prolate spheroids.

Funding. This work is supported by the Natural Science Foundation of China (Grant Nos.12388101, 92252104 and 9225220).

Declaration of Interests. The authors report no conflict of interest.

Appendix A. Validation of the numerical method

A.1. *Drafting-kissing-tumbling of two settling spheres*

To validate the PR-DNS method introduced in section 2, we simulate the DKT process of two settling spheres in a closed container (Glowinski *et al.* 2001; Breugem 2012). The flow configuration is introduced as follows. The container has a size of $L_x \times L_y \times L_z = [0, 1\text{cm}] \times [0, 4\text{cm}] \times [0, 1\text{cm}]$, and is filled with a Newtonian fluid with a density of $\rho_f = 1000\text{kg/m}^3$ and a kinematic viscosity of $\nu = 10^{-3}\text{m}^2/\text{s}$. The gravity is applied in the negative y direction with an acceleration of $g = 9.8\text{m/s}^2$. Two spheres with a diameter of $D = 0.167\text{cm}$ and a density of $\rho_p = 1140\text{kg/m}^3$ settle from rest in the container. The initial positions of the two particles are $\boldsymbol{x}_1 = (0.495\text{cm}, 3.16\text{cm}, 0.495\text{cm})$ (initially leading particle) and $\boldsymbol{x}_2 = (0.505\text{cm}, 3.5\text{cm}, 0.505\text{cm})$ (initially trailing particle). In the simulation, the computational domain (which is the same as the container) is discretized to $N_x \times N_y \times N_z = 96 \times 384 \times 96$ Eulerian grid cells, and the surface of the sphere is represented by $N_L = 731$ Lagrangian marker points. Figure 14 depicts the temporal evolution of the velocities of the two spheres during the DKT process. We observe that the initially trailing particle is accelerated to settle faster than the leading particle from $t \approx 0.15$s, and progressively approaches the leading particle (drafting stage). At around $t \approx 0.34$s, the two particles get touched (kissing stage) and then separate (tumbling stage). As shown in figure 14, the velocities of two particles calculated by the present simulation are in agreement with the reference (Breugem 2012) in the drafting stage. While, there is a slight discrepancy between the present result and the reference data after the collision of the two spheres, which is attributed to the difference in the collision model used here and in Breugem (2012).

A.2. *Grid-dependence test: sedimentation of an isolated prolate particle*

In this section, we simulate the settling motion of an isolated prolate particle, and examine the influence of grid resolution on the simulation results. The prolate particle with the same parameters as in the main text (i.e. $\lambda = 3$, $Ga = 80$, $\alpha = 2$) is considered. To simulate the

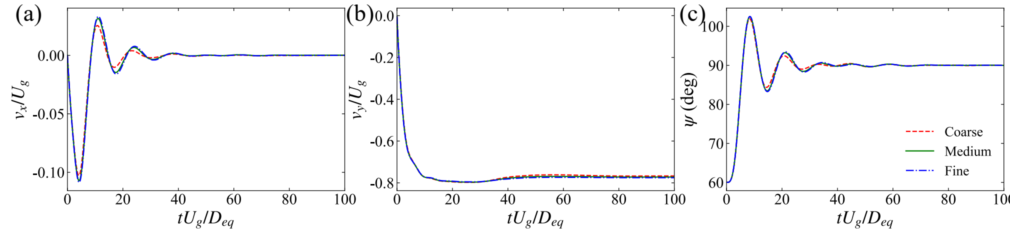

Figure 15: Time evolution of the (a) horizontal velocity, (b) vertical velocity and (c) pitch angle of the isolated prolate spheroid settling in a initially quiescent fluid. The characteristic velocity $U_g = \sqrt{(\alpha - 1)gD_{eq}}$ is used for the normalization.

settling motion of the isolate prolate particle in the initially quiescent fluid, a computational domain with a size of $L_x \times L_y \times L_z = 12D_{eq} \times 24D_{eq} \times 12D_{eq}$ is utilized, and the moving domain method (Chen *et al.* 2019) is adopted that the computational domain moves in accordance with the downward motion of the particle to save the computational cost. We impose a Dirichlet boundary condition with zero velocity on the bottom boundary, and impose a Neumann boundary condition on the upper boundary of the computational domain. In the lateral directions, the periodic boundary condition is applied. In the simulation, the prolate particle is released from rest with an initial pitch angle of $\psi_0 = 60°$ ($\boldsymbol{n}_0 = (\sqrt{3}/2, 0.5, 0)$). Three simulations with different grid resolutions are conducted, i.e. $\Delta h_{coarse} = D_{eq}/16$, $\Delta h_{medium} = D_{eq}/24$ and $\Delta h_{fine} = D_{eq}/32$. The results of the three simulations are depicted in figure 15. The discrepancy between the results obtained by the intermediate and fine grid is negligible. Therefore, the resolution of $\Delta h = D_{eq}/24$ is sufficient to resolve the prolate spheroid, and is thus adopted in the simulations in the main text. In addition, as shown in figure 15 (c), the prolate spheroid re-orientates to the broad-side-on alignment with $\psi = 90°$ as the steady orientation. The terminal settling velocity is $V_t = 0.772U_g$, yielding a Reynolds number of $Re_t = V_t D_{eq}/\nu = 61.8$.

REFERENCES

Anoukou, K., Brenner, R., Hong, F., Pellerin, M. & Danas, K. 2018 Random distribution of polydisperse ellipsoidal inclusions and homogenization estimates for porous elastic materials. *Comput. Struct.* **210**, 87–101.

Ardekani, M. N., Costa, P., Breugem, W. P. & Brandt, L. 2016 Numerical study of the sedimentation of spheroidal particles. *Int. J. Multiph. Flow* **87**, 16–34.

Ayala, O., Rosa, B. & Wang, L.-P. 2008 Effects of turbulence on the geometric collision rate of sedimenting droplets. part 2. theory and parameterization. *New J. Phys.* **10** (7), 075016.

Breugem, W.-P. 2012 A second-order accurate immersed boundary method for fully resolved simulations of particle-laden flows. *J. Comput. Phys.* **231** (13), 4469–4498.

Chen, S.-H., Ku, Y. & Lin, C.-A. 2019 Simulations of settling object using moving domain and immersed-boundary method. *Comput. fluids* **179**, 735–743.

Chrust, M., Bouchet, G. & Dušek, J. 2013 Numerical simulation of the dynamics of freely falling discs. *Phys. Fluids* **25** (4), 044102.

Costa, P., Boersma, B. J., Westerweel, J. & Breugem, W.-P. 2015 Collision model for fully resolved simulations of flows laden with finite-size particles. *Phys. Rev. E* **92** (5), 053012.

Dabade, V., Marath, N. K. & Subramanian, G. 2016 The effect of inertia on the orientation dynamics of anisotropic particles in simple shear flow. *J. Fluid Mech.* **791**, 631–703.

Di Felice, R. 1999 The sedimentation velocity of dilute suspensions of nearly monosized spheres. *Int. J. Multiph. Flow* **25** (4), 559–574.

Ern, P., Risso, F., Fabre, D. & Magnaudet, J. 2012 Wake-induced oscillatory paths of bodies freely rising or falling in fluids. *Annu. Rev. Fluid Mech.* **44** (1), 97–121.

Eshghinejadfard, A., Abdelsamie, A., Janiga, G. & Thévenin, D. 2016 Direct-forcing immersed boundary lattice boltzmann simulation of particle/fluid interactions for spherical and non-spherical particles. *Particuology* **25**, 93–103.

Ferenc, J. & Néda, Z. 2007 On the size distribution of poisson voronoi cells. *Physica A: Statistical Mechanics and its Applications* **385** (2), 518–526.

Fornari, W., Ardekani, M. N. & Brandt, L. 2018 Clustering and increased settling speed of oblate particles at finite reynolds number. *J. Fluid Mech.* **848**, 696–721.

Fortes, A. F., Joseph, D. D. & Lundgren, T. S. 1987 Nonlinear mechanics of fluidization of beds of spherical particles. *J. Fluid Mech.* **177**, 467–483.

Garside, J. & Al-Dibouni, M. R. 1977 Velocity-voidage relationships for fluidization and sedimentation in solid-liquid systems. *Ind. Eng. Chem. Process. Des. Dev.* **16** (2), 206–214.

Glowinski, R., Pan, T.W., Hesla, T.I., Joseph, D.D. & Périaux, J. 2001 A fictitious domain approach to the direct numerical simulation of incompressible viscous flow past moving rigid bodies: Application to particulate flow. *J. Comput. Phys.* **169** (2), 363–426.

Guazzelli, É. & Hinch, J. 2011 Fluctuations and instability in sedimentation. *Annu. Rev. Fluid Mech.* **43** (1), 97–116.

Happel, J. & Brenner, H. 1983 *Low Reynolds Number Hydrodynamics*. United States: D. Reidel Publishing Co.,Hingham, MA.

Horowitz, M. & Williamson, C. H. K. 2010 The effect of reynolds number on the dynamics and wakes of freely rising and falling spheres. *J. Fluid Mech.* **651**, 251–294.

Huisman, S. G., Barois, T., Bourgoin, M., Chouippe, A., Doychev, T., Huck, P., Morales, C. E. B., Uhlmann, M. & Volk, R. 2016 Columnar structure formation of a dilute suspension of settling spherical particles in a quiescent fluid. *Phys. Rev. Fluids* **1** (7), 074204.

Iaccarino, G. & Mittal, R. 2004 Immersed boundary method. *Annu. Rev. Fluid Mech.* **37** (37), 239–261.

Jeffrey, D. J. 1982 Low-reynolds-number flow between converging spheres. *Mathematika* **29** (1), 58–66.

Jenny, M., Duek, J. & Bouchet, G. 2004 Instabilities and transition of a sphere falling or ascending freely in a newtonian fluid. *J. Fluid Mech.* **508**, 201–239.

Jucha, J., Naso, A., Lévêque, E. & Pumir, A. 2018 Settling and collision between small ice crystals in turbulent flows. *Phys. Rev. Fluids* **3** (1), 014604.

Kajishima, T. 2004 Influence of particle rotation on the interaction between particle clusters and particle-induced turbulence. *Int. J. Heat Fluid Flow* **25** (5), 721–728.

Kajishima, T. & Takiguchi, S. 2002 Interaction between particle clusters and particle-induced turbulence. *Int. J. Heat Fluid Flow* **23** (5), 639–646.

Kempe, T. & Fröhlich, J. 2012 An improved immersed boundary method with direct forcing for the simulation of particle laden flows. *J. Comput. Phys.* **231** (9), 3663–3684.

Khayat, R. E. & Cox, R. G. 1989 Inertia effects on the motion of long slender bodies. *J. Fluid Mech.* **209**, 435–462.

Kim, K., Baek, S.-J. & Sung, H. J. 2002 An implicit velocity decoupling procedure for the incompressible navier-stokes equations. *Int. J. Numer. Methods Fluids* **38** (2), 125–138.

Koch, D. L. & Hill, R. J. 2001 Inertial effects in suspension and porous-media flows. *Annu. Rev. Fluid Mech.* **33** (1), 619–647.

Kuusela, E., Lahtinen, J. M. & Ala-Nissila, T. 2003 Collective effects in settling of spheroids under steady-state sedimentation. *Phys. Rev. Lett.* **90** (9), 094502.

Lu, J., Xu, X., Zhong, S., Ni, R. & Tryggvason, G. 2023 The dynamics of suspensions of prolate spheroidal particles—effects of volume fraction. *Int. J. Multiph. Flow* **165**, 104469.

Mallios, S. A., Drakaki, E. & Amiridis, V. 2020 Effects of dust particle sphericity and orientation on their gravitational settling in the earth's atmosphere. *J. of Aerosol Sci.* **150**, 105634.

Monchaux, R., Bourgoin, M. & Cartellier, A. 2010 Preferential concentration of heavy particles: A voronoï analysis. *Phys. Fluids* **22** (10), 103304.

Moriche, M., Hettmann, D., García-Villalba, M. & Uhlmann, M. 2023 On the clustering of low-aspect-ratio oblate spheroids settling in ambient fluid. *J. Fluid Mech.* **963**, A1.

Peskin, C. S. 2002 The immersed boundary method. *Acta Numer.* **11**, 479–517.

Pruppacher, H.R. & Klett, J.D. 2010 *Microphysics of Clouds and Precipitation*, chap. 11.6. Springer Netherlands.

Richardson, J.F. & Zaki, W.N. 1954 The sedimentation of a suspension of uniform spheres under conditions of viscous flow. *Chem. Eng. Sci* **3** (2), 65–73.

Roma, A. M., Peskin, C. S. & Berger, M. J. 1999 An adaptive version of the immersed boundary method. *J. Comput. Phys.* **153** (2), 509–534.

SAINTILLAN, D., SHAQFEH, E. S. G. & DARVE, E. 2006 The growth of concentration fluctuations in dilute dispersions of orientable and deformable particles under sedimentation. *J. Fluid Mech.* **553**, 347–388.

SHAW, R. A. 2003 Particle-turbulence interactions in atmospheric clouds. *Annu. Rev. Fluid Mech.* **35** (1), 183–227.

SHIN, M., KOCH, D. L. & SUBRAMANIAN, G. 2009 Structure and dynamics of dilute suspensions of finite-reynolds-number settling fibers. *Phys. Fluids* **21** (12), 123304.

SIEWERT, C., KUNNEN, R. P. J. & SCHRÖDER, W. 2014 Collision rates of small ellipsoids settling in turbulence. *J. Fluid Mech.* **758**, 686–701.

SLOMKA, J. & STOCKER, R. 2020 On the collision of rods in a quiescent fluid. *Proc. Natl. Acad. Sci.* **117** (7), 3372–3374.

TRUDNOWSKA, E., LACOUR, L., ARDYNA, M., ROGGE, A., IRISSON, J. O., WAITE, A. M., BABIN, M. & STEMMANN, L. 2021 Marine snow morphology illuminates the evolution of phytoplankton blooms and determines their subsequent vertical export. *Nat. Commun.* **12** (1), 2816.

UHLMANN, M. 2005 An immersed boundary method with direct forcing for the simulation of particulate flows. *J. Comput. Phys.* **209** (2), 448–476.

UHLMANN, M. & DOYCHEV, T. 2014 Sedimentation of a dilute suspension of rigid spheres at intermediate galileo numbers: The effect of clustering upon the particle motion. *J. Fluid Mech.* **752**, 310–348.

VOTH, G. A. & SOLDATI, A. 2017 Anisotropic particles in turbulence. *Annu. Rev. Fluid Mech.* **49** (1), 249–276.

WANG, H., ZHANG, B., LI, X., XIAO, Y. & YANG, C. 2022 Modeling total drag force exerted on particles in dense swarm from experimental measurements using an inline image-based method. *Chem. Eng. J.* **431**, 133485.

WANG, L.-P., AYALA, O., KASPRZAK, S. E. & GRABOWSKI, W. W. 2005 Theoretical formulation of collision rate and collision efficiency of hydrodynamically interacting cloud droplets in turbulent atmosphere. *J. Atmos. Sci.* **62** (7), 2433–2450.

WANG, L.-P., WEXLER, A. S. & ZHOU, Y. 2000 Statistical mechanical description and modelling of turbulent collision of inertial particles. *J. Fluid Mech.* **415**, 117–153.

YIN, X. & KOCH, D. L. 2007 Hindered settling velocity and microstructure in suspensions of solid spheres with moderate reynolds numbers. *Phys. Fluids* **19** (9), 093302.

ZAIDI, A. A. 2018*a* Particle resolved direct numerical simulation of free settling particles for the study of effects of momentum response time on drag force. *Powder Technol.* **335**, 222–234.

ZAIDI, A. A. 2018*b* Particle velocity distributions and velocity fluctuations of non-brownian settling particles by particle-resolved direct numerical simulation. *Physical Review E* **98** (5), 053103.

ZAIDI, A. A., TSUJI, T. & TANAKA, T. 2014 Direct numerical simulation of finite sized particles settling for high reynolds number and dilute suspension. *Int. J. Heat Fluid Flow* **50**, 330–341.

ZAIDI, A. A., TSUJI, T. & TANAKA, T. 2015 Direct numerical simulations of inertial settling of non-brownian particles. *Korean J. Chem. Eng.* **32** (4), 617–628.

ZHOU, W., CHRUST, M. & DUŠEK, J. 2017 Path instabilities of oblate spheroids. *J. Fluid Mech.* **833**, 445–468.